

Communication

Enhanced CO₂ Photoreduction over Bi₂Te₃/TiO₂ Nanocomposite via a Seebeck Effect

Yiming Lei ^{1,2} , Zewei Jia ^{1,2}, Huilin Hu ^{1,2}, Lequan Liu ^{1,2}, Jinhua Ye ^{1,2,3} and Defa Wang ^{1,2,*}

¹ TJU-NIMS International Collaboration Laboratory, Key Laboratory of Advanced Ceramics and Machining Technology (Ministry of Education), Tianjin Key Laboratory of Composite and Functional Materials, School of Material Science and Engineering, Tianjin University, Tianjin 300072, China

² Collaborative Innovation Centre of Chemical Science and Engineering (Tianjin), Tianjin 300072, China

³ International Center for Materials Nanoarchitectonics (WPI-MANA), National Institute for Materials Science (NIMS), 1-1 Namiki, Tsukuba 305-0044, Japan

* Correspondence: defawang@tju.edu.cn; Tel.: +86-022-27405065

Abstract: The activation of carbon dioxide (CO₂) molecules and separation/transfer of photoinduced charge carriers are two crucial factors influencing the efficiency of CO₂ photoreduction. Herein, we report a p-type Bi₂Te₃/commercial TiO₂ (pBT/P25) nanocomposite for enhanced CO₂ photoreduction. Upon light irradiation, a temperature gradient formed in pBT induces the Seebeck effect to build a thermoelectric field, which promotes the charge carriers' separation/transfer. Additionally, pBT with a strong light absorption capacity generates the photothermal effect favoring the activation of CO₂ molecules. In addition, the excellent electric conductivity and large work function render pBT an efficient cocatalyst for further improving the charge carriers' separation/transfer. Owing to the synergistic enhancement effect of pBT on the activation of CO₂ molecules and promotion of charge separation/transfer, we achieved the highest CO evolution rate over pBT(2)/P25 of 19.2 μmol·g_{cat}⁻¹·h⁻¹, which was approximately 5.5 times that of bare P25. This work suggests that a thermoelectric material/semiconductor nanocomposite could be developed as an efficient photo-thermo-electro-chemical conversion system for enhanced CO₂ reduction via promoting the charge carriers' separation/transfer.

Keywords: TiO₂; Bi₂Te₃; Seebeck effect; CO₂ photoreduction; charge separation



Citation: Lei, Y.; Jia, Z.; Hu, H.; Liu, L.; Ye, J.; Wang, D. Enhanced CO₂ Photoreduction over Bi₂Te₃/TiO₂ Nanocomposite via a Seebeck Effect. *Catalysts* **2022**, *12*, 1323. <https://doi.org/10.3390/catal12111323>

Academic Editor: Ewa Kowalska

Received: 28 September 2022

Accepted: 24 October 2022

Published: 27 October 2022

Publisher's Note: MDPI stays neutral with regard to jurisdictional claims in published maps and institutional affiliations.



Copyright: © 2022 by the authors. Licensee MDPI, Basel, Switzerland. This article is an open access article distributed under the terms and conditions of the Creative Commons Attribution (CC BY) license (<https://creativecommons.org/licenses/by/4.0/>).

1. Introduction

The utilization of fossil fuels leads to the emission of ~1.3 × 10⁴ million tons of carbon dioxide (CO₂) in the atmosphere per year, which is one of the reasons for global warming and the greenhouse effect [1,2]. Converting CO₂ into high-value-added chemicals has become the best choice for its commercial application. Nonetheless, CO₂ conversion reactions usually require a high energy input [3]. Thus, it is of great significance to develop a reliable CO₂ conversion path under the condition of low energy consumption. As an ideal green technology for solar-to-chemical conversion, the photoreduction of CO₂ into hydrocarbon solar fuels with sunlight as the sole input energy source has been attracting a great deal of research interest in recent years [4–9]. In those possible CO₂ photoreduction products, CO can be utilized as both a Fischer-Tropsch synthesis reaction feed gas and a reducing agent in metal smelting [10,11]. In this context, the reduction of CO₂ to toxic CO for various industrial applications is a promising strategy for solving the two globally concerning issues of the energy crisis and greenhouse effects. Among many photocatalysts, TiO₂ has been widely studied for water splitting [12], the degradation of organic pollutants [13], and CO₂ photoreduction [14] due to its low price, non-toxic property, and stability. However, it is still a tough challenge to achieve a high photoconversion efficiency because of the extremely thermodynamically stable non-polar CO₂ molecules and the fast recombination of photogenerated electron–hole pairs over the TiO₂ surface [15–17].

On one hand, to promote the adsorption/activation of CO₂ molecules, the significant role of the photothermal effect has been paid extensive attention, because the high photothermal temperature is believed to greatly favor the expansion of light absorbance and more importantly the activation of the CO₂ molecules, thereby leading to a significantly enhanced CO₂ photoreduction performance [18–21]. On the other hand, to suppress the rapid recombination of photoexcited charge carriers, one effective solution is to introduce co-catalysts, including noble metals [22–24], noble-metal-contained alloys, or core-shell structured bimetals [25–29]. Additionally, our lab recently developed the alkalinized Ti₃C₂ as an excellent noble-metal-free cocatalyst for significantly enhancing the photocatalytic CO₂ reduction of commercial TiO₂ (P25) [30,31]. In principle, the large work function and excellent electrical conductivity of a cocatalyst favor the separation of photo-generated electrons and holes and thus achieve a high activity of CO₂ photoreduction [23,24].

In addition to using cocatalysts, previous studies have shown that electric/magnetic fields could serve as the driving force for effectively promoting the separation/transfer of photoexcited charge carriers and hence increasing the photocatalytic activities. For instance, some researchers found that the oppositely charged ends of tourmaline could drive electrons and holes to transfer in opposite directions to enhance the photocatalytic activity of dye or isopropanol (IPA) degradation [32,33]. Moreover, the non-toxic Fe₃O₄ was selected as an appropriate supplier of a magnetic field in a TiO₂-based photocatalyst with enhanced charge separation, thus resulting in significantly increased photocatalytic activities [34,35].

It is known that most thermoelectric materials possess a strong absorption capacity, which can make full use of ultraviolet–visible–infrared (UV–Vis–IR) light to produce the photothermal effect [36]. In addition to the photothermal effect, thermoelectric materials are able to induce an electric field by a temperature gradient, which is generally known as the Seebeck effect. Previously, the applications of various thermoelectric materials in photocatalysis have been reported, either by the thermoelectric material alone [37–40] or by combining the thermoelectric material with other wide bandgap semiconductors to form the type-II heterostructure [41–43]. To the best of our knowledge, however, the aforementioned Seebeck effect has never been used for enhancing photocatalytic activity. As one of the common thermoelectric materials, the excellent optical, electrical, and thermoelectric properties of the black bismuth telluride (Bi₂Te₃) would render the formation of the photothermal effect upon light irradiation. Meanwhile, if Bi₂Te₃ is combined with a suitable semiconductor and the Bi₂Te₃/semiconductor composite is subjected to light irradiation, a photothermal effect and a temperature gradient could be formed, inducing a thermoelectric field in Bi₂Te₃ via the Seebeck effect [44]. Moreover, Bi₂Te₃ could also serve as a cocatalyst for CO₂ reduction owing to its excellent electrical conductivity and high work function (~5.3 eV, close to the Fermi-level of Bi₂Te₃) [45]. In this context, Bi₂Te₃ is believed to play a critical role in activating the CO₂ molecules and promoting the separation/transfer of photoinduced charge carriers, thus significantly enhancing the CO₂ photoreduction performance.

Herein, we report a Bi₂Te₃/TiO₂ nanocomposite, showing significantly enhanced CO₂ photoreduction activity. With the intention of CO₂ reduction, we purposely selected the p-type Bi₂Te₃ (pBT), from which the thermoelectric field would be favorable for driving the photogenerated electrons from TiO₂ to the pBT surface to participate in the CO₂ reduction reaction. On the one hand, a temperature gradient formed in pBT induces a thermoelectric field via the Seebeck effect, favoring the separation/transfer of photoinduced electrons and holes. On the other hand, the strong light absorption capacity of pBT offers an efficient photo-thermal conversion to produce a high temperature on the pBT surface, which facilitates the activation of CO₂ molecules. Moreover, the interfacial electronic interaction in pBT/P25 endows pBT as a cocatalyst with the electron-rich environment for increasing CO₂ photoreduction. Hence, the pBT/P25 nanocomposite exhibited a CO evolution rate of 19.2 μmol·g_{cat}⁻¹·h⁻¹, approximately 5.5 times that of bare P25. Our research demonstrates that the thermoelectric effect could be incorporated into the strategy for developing an

efficient photo-thermo-electro-chemical conversion system for CO₂ reduction based on a full-spectrum-responsive thermoelectric material/semiconductor nanocomposite.

2. Results and Discussion

2.1. Structural, Morphological, and Optical Characterizations

As shown in Figure 1a, the XRD pattern of pBT(2)/P25 could be indexed well by the joint committee on powder diffraction standards (JCPDS) card of Bi₂Te₃ [15] and dual-phased P25 [46]. Three main peaks at 25.3, 37.4, and 47.8 were typical for the (101), (004), (200) planes of anatase TiO₂ (JCPDS No. 21-1272), and the peaks at 27.4, 36.0, and 41.2 could be assigned to (110), (111), and (220) planes of rutile TiO₂ (JCPDS No. 21-1276). The peaks at 27.7°, 37.8°, and 44.7° corresponded to the (015), (1010), and (110) planes of Bi₂Te₃ (JCPDS No. 15-0863). TEM images showed uniform spherical P25 nanoparticles with a diameter of ~25 nm, and pBT nanoparticles with a diameter of ~10 nm (Figure S1). The HRTEM image, as shown in Figure 1b displayed that the distances of lattice fringes were 0.322, 0.352, and 0.249 nm, and in accordance with the (015) planar space of pBT, (101) planar spaces of anatase, and rutile TiO₂, respectively [46]. The high-angle annular dark-field (HAADF) TEM image and corresponding EDS analysis results show the existence of Ti, O, Bi, and Te elements in pBT(2)/P25 (Figure S2). The above results indicate that the pBT nanoparticles were loaded on P25 with an excellent interfacial structure, which was beneficial for the charge-carrier transfer, as will be discussed below.

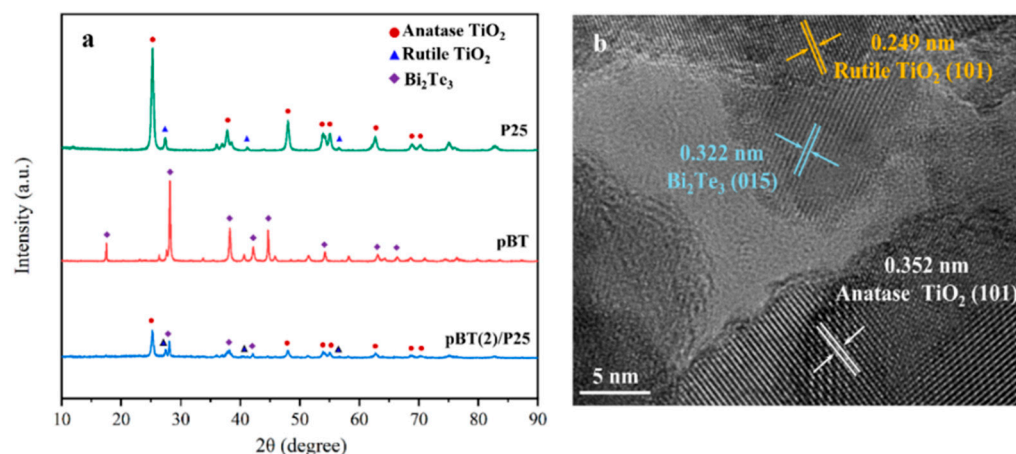


Figure 1. (a) XRD patterns of P25, pBT, and pBT(2)/P25; (b) HRTEM image of pBT(2)/P25.

The SEM images of P25 and pBT(2)/P25 showed that the diameter of P25 in pBT(2)/P25 was maintained at ~25 nm after hydrothermal treatment (Figure S3). Moreover, we studied the Brunauer-Emmett-Teller (BET) surface area of P25 and pBT(2)/P25 using N₂ sorption analysis. As shown in Figure S4, the N₂ sorption isotherm of pBT(2)/P25 did not exhibit an apparent difference in comparison to that of P25. The specific surface area of P25 and pBT(2)/P25 was 57.6 and 54.9 m²·g⁻¹, respectively. Although the efficiency of surface redox reactions could be dictated by the morphology of photocatalysts or the number of surface reduction/oxidation reactive sites, such similar results of P25 and pBT(2)/P25 in the structure/morphology and specific surface area could not lead to the significantly enhanced CO₂ photoreduction activity of pBT(2)/P25 as shown below.

The XPS survey spectrum of pBT(2)/P25 showed the peaks of Ti 2p, O 1s, Bi 4f, and Te 3d (Figure S5). In the high-resolution XPS spectra, we observed that the two peaks of Ti 2p_{3/2} and Ti 2p_{1/2} in pBT(2)/P25 were shifted to higher energies (463.90 and 458.20 eV) than those in pure P25 (463.75 and 458.15 eV, Figure S6a) while the peaks of O 1s were almost unchanged (529.50 eV, Figure S6b). The peaks of Bi 4f_{7/2} and Bi 4f_{5/2} in pBT(2)/P25 were shifted to lower energies (159.00 and 164.30 eV) than those in pure pBT (159.20 and 164.60 eV, Figure S6c) [47]. Similarly, the peaks of Te 3d_{5/2} Te 3d_{3/2} in pBT(2)/P25 were shifted to lower energies (575.70 and 586.10 eV) than those in pure pBT (576.15 and

586.40 eV), and besides, an oxide peak of Te 3d at ~ 580.30 eV was observed in pBT(2)/P25 (Figure S6d). The shift of binding energies strongly suggested the electronic coupling of pBT and P25 [48,49], which might form an electron-rich environment in pBT favoring CO_2 reduction [31].

The UV–Vis–IR DRS spectra in Figure 2a showed that compared with pure P25 only absorbing UV light due to the wide bandgap (~ 3.2 eV) [30], the absorbance of pBT(2)/P25 was appreciably enhanced, especially in the Vis–IR range because of the strong light absorption ability of loaded pBT nanoparticles. As expected, the strong light absorption ability of pBT would result in quite high photothermal temperature in pBT(x)/P25 depending on the loaded amount of pBT. The in situ monitored photothermal temperatures on the surfaces of P25, pBT, and pBT(x)/P25 ($x = 1, 2, 3, 4$) upon a 300 W Xe lamp irradiation are shown in Figure 2b. The photothermal temperatures for all the samples increased with the increasing irradiation time and became gradually saturated after approximately 30 min. The photothermal temperatures for P25 and pBT were 120 °C and 350 °C, respectively. As for the pBT(x)/P25 ($x = 1, 2, 3, 4$) composites, the photothermal temperatures were between 150 and 250 °C. The greater the mass percentage of pBT, the higher photothermal temperature would be. The high photothermal temperature might be one of the important reasons accounting for the enhanced CO_2 photoreduction performance of pBT(2)/P25, as discussed below.

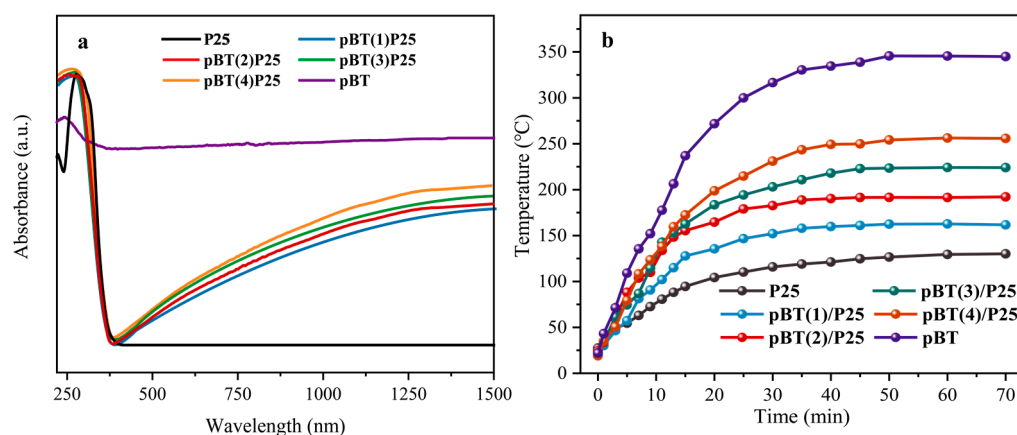


Figure 2. (a) UV–vis–NIR spectra of pBT, pBT(x)/P25 ($x = 1, 2, 3, 4$), and P25; (b) In situ monitoring of the photothermal temperatures over P25, pBT(x)/P25, and pBT.

2.2. Temperature Gradient and Electric Potential Simulation

A temperature gradient was necessary for the Seebeck effect of pBT to induce a built-in electric field. In practice, it was hard to measure the temperature gradient in pBT/P25. Instead, the temperature gradient in pBT/P25 nanocomposite was theoretically simulated by a commercial FEM solver in COMSOL Multiphysics according to Equation (1) [44,49]. Considering the fact that the thermal conductivities of TiO_2 ($\sim 8.50 \text{ W m}^{-1} \cdot \text{K}^{-1}$) and Bi_2Te_3 ($\sim 1.47 \text{ W m}^{-1} \cdot \text{K}^{-1}$) are different [50,51], and the heat-dissipating from Bi_2Te_3 of higher temperature to TiO_2 of lower temperature was faster than that to a CO_2 atmosphere, a temperature gradient could be formed between the exposed surface of Bi_2Te_3 and the interface of $\text{Bi}_2\text{Te}_3/\text{TiO}_2$. As shown in Figure 3a, the simulated temperature distribution verified the formation of a temperature gradient in a $\text{Bi}_2\text{Te}_3/\text{TiO}_2$ nanocomposite under light irradiation. The temperature gradient over Bi_2Te_3 could be ~ 40 °C, meaning the Seebeck effect could be excited in $\text{Bi}_2\text{Te}_3/\text{TiO}_2$ via light illumination [44,52].

In principle, the Seebeck effect suggested that an electric field will be formed by the majority carrier transfer from the high-temperature end to the low-temperature end in a thermoelectric material [53]. For p-type Bi_2Te_3 (pBT), the majority carrier (holes) would diffuse from the high-temperature end (exposed surface of pBT) to the low-temperature end (interface of pBT/P25), inducing an electric field in the same direction as the directional diffusion of holes. The COMSOL software displayed the electric potential over Bi_2Te_3

according to the above-simulated temperature gradient. Figure 3b showed that the electric potential was ~ 7.85 V. The direction of the thermoelectric field was from the high electric potential surface (high-temperature surface of pBT) to the low electric potential surface (interface of pBT/P25). Thus, we expected that the Seebeck effect would undoubtedly influence the CO_2 photoreduction process of pBT/P25 by accelerating the transfer of photoinduced electrons.

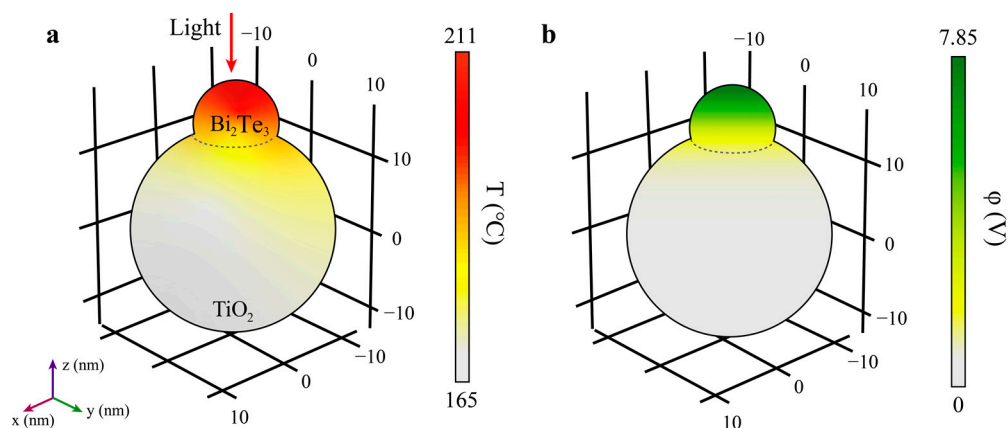


Figure 3. Simulated (a) temperature distribution and (b) electric potential over pBT(2)/P25 nanocomposite upon a single-wavelength ($\lambda = 800$ nm) light irradiation.

2.3. CO_2 Photoreduction Performances

The GC spectra were obtained to determine the products of CO_2 photoreduction over pBT(2)/P25. As shown in Figure S7, we observed that the main reduction product was CO with an evolution rate of $19.2 \mu\text{mol}\cdot\text{g}_{\text{cat}}^{-1}\cdot\text{h}^{-1}$. In addition, CH_4 and H_2 were also detected as the reduction products with much lower evolution rates of $0.4 \mu\text{mol}\cdot\text{g}_{\text{cat}}^{-1}\cdot\text{h}^{-1}$ and $2.1 \mu\text{mol}\cdot\text{g}_{\text{cat}}^{-1}\cdot\text{h}^{-1}$, respectively. O_2 was detected as the oxidation product of H_2O with an evolution rate of $9.6 \mu\text{mol}\cdot\text{g}_{\text{cat}}^{-1}\cdot\text{h}^{-1}$, indicating that the CO_2 photoreduction over pBT/P25 was a complete redox reaction. Considering the aforementioned results, we used the CO evolution rate to evaluate the CO_2 photoreduction activities of P25 and pBT(x)/P25 ($x = 1, 2, 3, 4$).

As displayed in Figure 4a, the pure pBT showed almost no activity, and the pure P25 only exhibited a very low CO evolution rate of $3.5 \mu\text{mol}\cdot\text{g}_{\text{cat}}^{-1}\cdot\text{h}^{-1}$. Surprisingly, after loading pBT on P25, the as-obtained pBT(x)/P25 nanocomposites exhibited significantly increased activity compared with either pBT or P25. With an optimal pBT loading of 2 wt%, the pBT(2)/P25 composite showed the highest CO evolution rate of $19.2 \mu\text{mol}\cdot\text{g}_{\text{cat}}^{-1}\cdot\text{h}^{-1}$, which was nearly 5.5 times that of P25. Further increasing the pBT loading amount (e.g., pBT(3)/P25, and pBT(4)/P25) decreased the activity, probably due to the light-blocking effect of pBT that had almost no activity for CO_2 photoreduction. The O_2 evolution rates were shown in Figure 4b. Additionally, pBT(2)/P25 had the highest activity, which was ~ 5.1 times higher than that of P25 ($1.9 \mu\text{mol}\cdot\text{g}_{\text{cat}}^{-1}\cdot\text{h}^{-1}$). As mentioned above, the enhanced CO_2 photoreduction performance of pBT/P25 could be partially attributed to the high photothermal temperature over the pBT (e.g., ~ 193 °C for pBT(2)/P25) and thermoelectric field in pBT upon light irradiation.

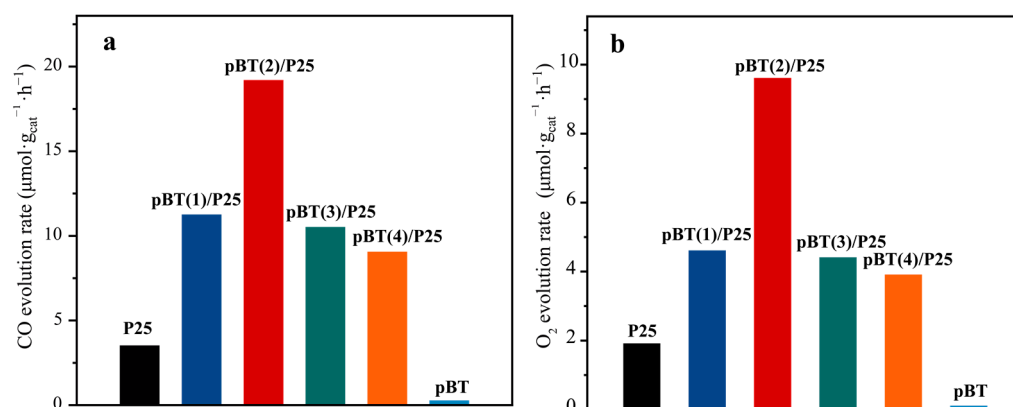


Figure 4. (a) CO and (b) O₂ evolution rates over P25, pBT(x)/P25, and pBT under a 300 W full-arc Xe lamp illumination.

To verify the important role of the photothermal effect and the Seebeck effect in improving the activity of pBT(2)/P25 for CO₂ photoreduction, we carried out several experiments as follows. The thermocatalytic reaction over pBT(2)/P25 was conducted in the dark using a flexible electric heating jacket to heat the reaction cell at ~193 °C. The performance of thermal catalysis ($0.2 \mu\text{mol}\cdot\text{g}_{\text{cat}}^{-1}\cdot\text{h}^{-1}$) was much lower than that of photocatalysis under irradiation (Figure S8). We also carried out a blank test of CO₂ photoreduction on pBT(2)/Al₂O₃ under the same conditions as on pBT(2)/P25. The photothermal temperature over pBT(2)/Al₂O₃ was very close to that over pBT(2)/P25 (Figure S9), but Al₂O₃ did not possess any photocatalytic activity. The CO evolution rate over pBT(2)/Al₂O₃ ($<0.1 \mu\text{mol}\cdot\text{g}_{\text{cat}}^{-1}\cdot\text{h}^{-1}$, Figure S8) was negligible in comparison with that over pBT(2)/P25. In addition, the CO₂ photoreduction was carried out over pBT(2)/P25 by using a Y44 cutoff filter to completely block UV light (denoted as Xe-Y44). In this case, P25 would not be excited to show any photocatalytic activity judging from the light spectrum of Xe-Y44 (Figure S10) and the absorption spectrum of P25 (Figure 2a). Under the Xe-Y44 irradiation, the photothermal temperature over pBT(2)/P25 reached ~173 °C (Figure S11). Surprisingly, only a very low CO evolution rate ($\sim 0.2 \mu\text{mol}\cdot\text{g}_{\text{cat}}^{-1}\cdot\text{h}^{-1}$, Figure S8) was obtained over pBT(2)/P25 under Xe-Y44 irradiation. The above results indicated that without photoexcitation of P25, only heating the pBT(2)/P25 catalyst to a high temperature could not improve the activity of pBT(2)/P25 for CO₂ photoreduction.

In addition, to further confirm the role of the Seebeck effect in enhancing the CO₂ photoreduction activity, we used commercial n-type Bi₂Te₃ (nBT) to prepare the nBT(2)/P25 nanocomposite as a comparison of pBT(2)/P25. It is worth pointing out that nBT and pBT had the same light absorption capacity (Figure 5a), so the in situ monitored photothermal temperature of nBT(2)/P25 (~192 °C) was almost the same as that of pBT(2)/P25 (~193 °C, Figure 5b). Interestingly, the CO evolution rate over nBT(2)/P25 ($11.1 \mu\text{mol}\cdot\text{g}_{\text{cat}}^{-1}\cdot\text{h}^{-1}$, Figure 5c) was much less than that over pBT(2)/P25 ($19.2 \mu\text{mol}\cdot\text{g}_{\text{cat}}^{-1}\cdot\text{h}^{-1}$). In contrast to pBT with holes as the majority carrier, electrons are the majority carrier in nBT. Upon light irradiation, the electrons would diffuse from the high-temperature end on the exposed surface of nBT to the low-temperature end at the interface of nBT/P25. Obviously, the thermoelectric field formed in nBT would inhibit the transfer of photoinduced electrons from P25 to the nBT surface. Therefore, the CO evolution rate over nBT(2)/P25 was much less than that over pBT(2)/P25. The difference in CO evolution rates over pBT(2)/P25 and nBT(2)/P25 clearly confirmed that the Seebeck effect enhanced CO₂ photoreduction via accelerating photoexcited charge-carrier separation. Actually, several works have proved the promotion of Bi₂Te₃ on the charge transfer over TiO₂ due to the thermoelectric properties, indicating that it is feasible to enhance the photocatalytic activity over the Bi₂Te₃/TiO₂ nanocomposite by inducing a thermoelectric field in Bi₂Te₃ via the Seebeck effect [54,55].

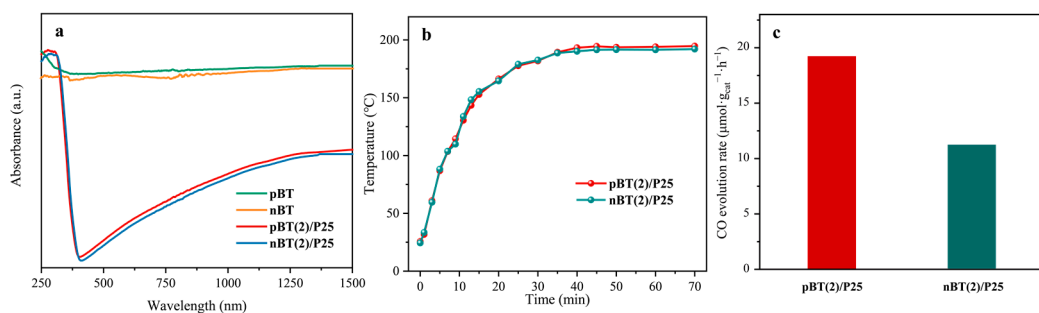


Figure 5. (a) UV-vis-IR spectra of pBT, nBT, pBT(2)/P25, and nBT(2)/P25; (b) In situ monitoring of the photothermal temperatures over pBT(2)/P25 and nBT(2)/P25; (c) CO evolution rates over pBT(2)/P25 and nBT(2)/P25 under a 300 W full-arc Xe lamp illumination.

On the other hand, we performed the CO₂ photoreduction experiment by putting the reaction cell in a basin containing cold water, just leaving the top window above the water level for passing through incident light. Under this circumstance, the photothermal temperature of pBT(2)/P25 (denoted pBT(2)/P25-Cool) under the full-arc Xe lamp irradiation was significantly reduced to ~84 °C (Figure S12, Table S1). We found that, as shown in Figure S13, the CO evolution rate over pBT(x)/P25-Cool was remarkably lower than that over pBT(x)/P25, however, the activity of P25-Cool had only a slight decline. The above results confirmed that the influence of the Seebeck effect on promoting charge transfer was weakened by the low-temperature because of the slight temperature gradient. Moreover, in consideration of the high photothermal temperature over the pBT surface, the above results also proved the photothermal effect of pBT on the enhanced activity of pBT(2)/P25 for CO₂ photoreduction, in the process of which the activation of CO₂ molecules by the high photothermal temperature played a crucial role. In fact, similar results were also reported in Ni-, Rh-, or Au-loaded SiO₂ and CeO₂ catalysts, in the interface of which the strong local electromagnetic field was formed to greatly favor the activation of CO₂ molecules [19,20,56].

Three cycles of reaction for a total of 6 h showed that there was almost no decrease in catalytic activity (Figure S14). The XRD patterns of pBT(2)/P25 before and after the reaction also showed no change (Figure S15). Additionally, the XPS spectra of pBT(2)/P25 showed that no new peak or obvious variation in the peak area ratio of four elements (Ti, O, Bi, and Te) in pBT(2)/P25 was observed after reactions, confirming the stability of pBT(2)/P25 (Figure S16). To clarify whether CO originated from CO₂ reduction, a series of blank experiments—as reported in previous studies—were conducted [57,58]. The reaction in the absence of pBT(2)/P25 catalyst (CO₂ and H₂O were added in the reaction cell) showed no evolution of CO or other hydrocarbons. When CO₂ and/or H₂O were not added or were replaced by Ar gas while keeping other conditions identical, no CO or other hydrocarbon was detected. These results exclude the possibility that the high yield of CO was from the adsorbed impurities containing carbon (if possible) on pBT(2)/P25.

2.4. Photoelectrochemical and Photoluminescence Properties

Previous results and discussion have proven the essential roles of the photothermal effect and the subsequent Seebeck effect of pBT in the significantly enhanced activity of pBT(2)/P25. Given the excellent electrical conductivity and large work function of pBT [45], we expected that pBT might also serve as a suitable cocatalyst in promoting the separation/transfer of photoexcited charge carriers. From this perspective, we carried out the photoelectrochemical (PEC) measurements of P25 and pBT(x)/P25, in the process of which the photothermal effect and Seebeck effect of pBT could be neglected since the surface temperatures of P25 and pBT(x)/P25 photoanodes immersed in the 0.5 M K₂SO₄ aqueous solution were in situ monitored to be only ~55.0 °C (Figure S17, Table S2). From Figure 6a, we could see that pBT(2)/P25 showed the highest transient photocurrent (TPC) intensity compared with P25 and other pBT(x)/P25 (x = 1, 3, 4) samples, corresponding to the

optimal photocatalytic activity. The pBT(2)/P25 also clearly showed the lowest PL intensity (Figure 6b), indicating a quenching effect of photoinduced electrons by pBT [59]. In no doubt, the photoelectrochemical and photoluminescence properties verified the significant role of pBT as an efficient cocatalyst in enhancing the CO₂ photoreduction performance of pBT(2)/P25. Additionally, we also utilized a UV lamp to completely exclude the Vis-NIR light, comparing the photocatalytic performance of P25 and pBT(2)/P25 (Figure S18). Under UV lamp illumination, the photothermal temperature over P25 and pBT(2)/P25 was enough low (~45 °C for P25-UV and 57 °C for pBT(2)/P25-UV, Figure S19) so that the Seebeck effect and photothermal effect were negligible. Additionally, the results show that the CO evolution rate over pBT(2)/P25 was still higher than that of P25, corresponding to the PEC results and confirming the enhancement effect of pBT as a cocatalyst. In fact, the work function of pBT (~5.3 eV) was similar to that of some noble metal cocatalysts (Pt~5.65 eV, Au~5.1 eV) [60]. The enrichment effect of the noble metal cocatalysts with a large work function on the photoexcited electrons from TiO₂ will transfer electrons to the cocatalysts and shift the Fermi energy level of the composites to a more negative point (closer to the conduction band of TiO₂), significantly improving the photocurrent intensity and reduction ability of the photogenerated electrons [61,62]. In this context, pBT as a cocatalyst not only promoted charge transfer efficiency but also enhanced the reduction ability of photoexcited electrons over pBT/P25.

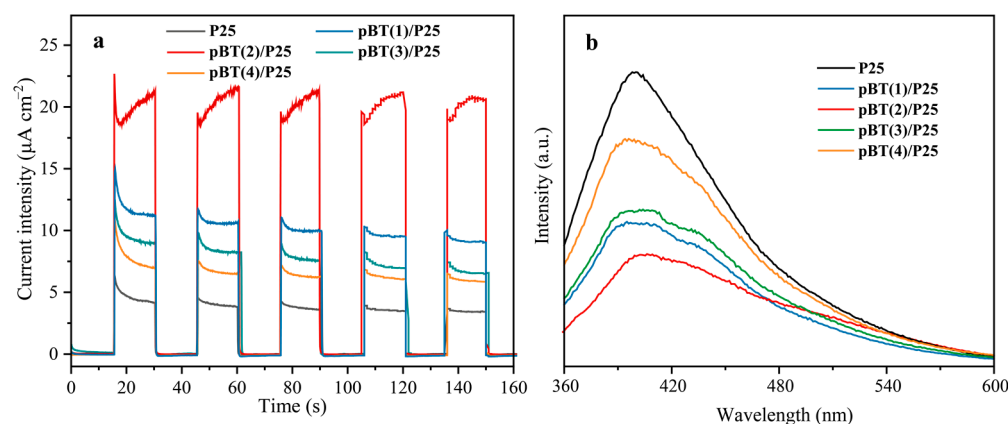


Figure 6. (a) Transient photocurrent responses of P25 and pBT(x)/P25 under a 300 W full-arc Xe lamp irradiation; and (b) photoluminescence spectra of P25 and pBT(x)/P25 with an excitation wavelength of $\lambda = 330$ nm.

Based on the above results and discussion, we could clarify that the thermoelectric effect, photothermal effect, and co-catalyzing effect of pBT were incorporated into the pBT/P25 nanocomposite with the promoted separation/transfer of photoinduced charge carriers, thereby realizing enhanced CO₂ photoreduction activity. Accordingly, we propose in Figure 7 a mechanism elucidating the enhanced CO₂ photoreduction over pBT/P25. Upon light irradiation, a temperature gradient is formed in pBT due to the non-uniform heat dissipation in pBT/P25. Then, the temperature gradient in pBT induces the Seebeck effect to create a built-in thermoelectric field, which drives the electrons excited from P25 to the pBT surface to participate in the CO₂ reduction. Meanwhile, the high photothermal temperature over the pBT surface benefits the thermodynamically endothermic CO₂ photoreduction by activating the CO₂ molecules. In addition, the excellent electric conductivity and large work function render pBT an efficient cocatalyst to improve the transfer and reduction ability of the photoinduced electrons for CO₂ reduction. Briefly, pBT plays an essential role in the separation/transfer of photoinduced charge carriers and the activation of CO₂ molecules, resulting in highly efficient CO₂ photoreduction over pBT/P25.

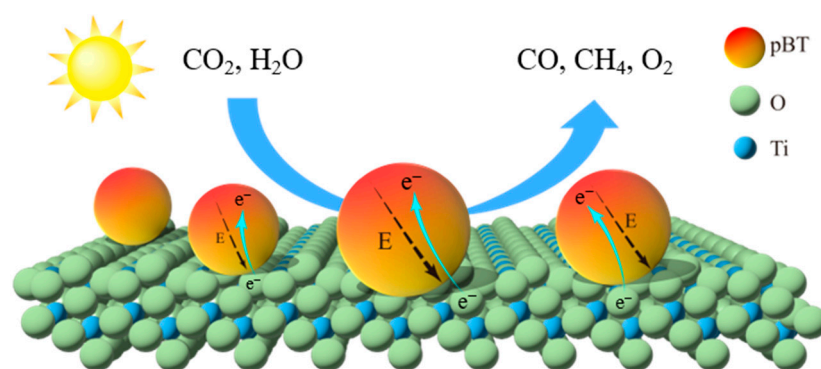


Figure 7. Enhancement mechanism for CO₂ photoreduction over pBT/P25 upon light irradiation.

3. Materials and Methods

3.1. Chemicals and Synthesis

Commercial TiO₂ (P25) (Sigma-Aldrich Co., Ltd., St. Louis, MO, USA), p-type Bi₂Te₃ (Iuding chemistry Co., Ltd., Hong Kong, China), n-type Bi₂Te₃ (Iuding chemistry Co., Ltd.), and CO₂ (99.99%, Tianjin Liufang Gas Co., Ltd., Tianjin, China) were used without further treatment.

The p-type Bi₂Te₃/P25 (pBT/P25) was synthesized using a hydrothermal method as follows: 500 mg of P25 and different amounts of p-type Bi₂Te₃ were mixed in 30 mL of Deionized (DI) water. After stirring for 30 min, the mixture was transferred into a 50 mL Teflon-lined stainless-steel autoclave and heated at 170 °C for 24 h. The resulting suspensions were completely washed with DI water and then dried in a vacuum oven at 60 °C for 12 h, obtaining pBT(x)/P25 (x = 1, 2, 3, 4 wt%; x is the weight ratio of pBT to P25) nanocomposites. Following the same procedure as mentioned above, we also prepared n-type Bi₂Te₃/P25 (nBT(2)/P25) for comparison.

Photoanode samples were fabricated by spin-coating the as-prepared catalysts on fluorine-doped SnO₂ (FTO) conductive glass. Typically, 10 mg of catalyst was dispersed in 5 mL of ethanol under ultrasonication. The slurry solution was spin-coated on FTO glass (10 × 10 mm²) for 60 cycles. After heating at 200 °C for 2 h, a photoanode sample was obtained.

3.2. Materials Characterization

The crystal phase was determined by X-ray diffraction (XRD; D8 Advanced, Bruker, Rheinstetten, Germany) using Cu-K_α radiation ($\lambda = 0.154178$ nm) at a scanning rate of 0.02°·s⁻¹. The morphology and microstructure of the samples were examined using transmission electron microscopy (TEM; Technai G2 F20, FEI, Eindhoven, The Netherlands). Ultraviolet-visible-infrared (UV-vis-IR) diffuse reflectance spectra (DRS) were recorded at room temperature on a spectrophotometer (UV-3600, Shimadzu, Kyoto, Japan) using BaSO₄ as a reference and converted to absorption spectra via the Kubelka-Munk (K-M) method. The chemical state was analyzed by X-ray photoelectron spectroscopy (XPS, Escalab 250Xi, Thermo Scientific, Waltham, MA, USA) calibrated by the C 1s peak (284.6 eV) of the surface adventitious carbon. Photoluminescence (PL) measurement was conducted on a fluorescence spectrometer (Fluorolog-3, Horiba Scientific, Piscataway, NJ, USA) with an excitation light wavelength of $\lambda = 330$ nm.

3.3. CO₂ Photoreduction Evaluation

The CO₂ photoreduction experiment was carried out in a reaction chamber with a quartz lid that secured the adequate transmittance of incident light. The reaction chamber with a total volume of 330 mL (OLPCRS-3, Shanghai Boyi Scientific Instrument Co. Ltd., Shanghai, China) was connected to a closed gas circulation system. Fifty milligrams of catalyst was uniformly dispersed on a porous quartzose slice, which was fixed on the stage inside the reactor. Three milliliters of DI water was injected into the cell as the

sacrificial agent and proton source for CO₂ photoreduction. After the reactor was sealed and evacuated, CO₂ gas was injected until a pressure of 70 kPa. A 300 W full-arc xenon lamp was employed as the light source, and the incident light intensity was measured to be $\sim 1.3 \text{ W} \cdot \text{cm}^{-2}$ using an optical power meter (THORLABS, PM 100D, Bergkirchen, Germany). The sample surface temperature was in situ monitored using an infrared thermometer (UT3021, UNI-T Co., Ltd., Dongguan, China), which was pre-calibrated using a reflectance coefficient of 0.36.

During the reaction, a gaseous sample (0.5 mL) was periodically taken from the reaction vessel and analyzed on a gas chromatograph (GC-2014, Shimadzu, Kyoto, Japan) equipped with a flame ionization detector (FID) for analysis of CO and CH₄, and a methanizer for an analysis of CO₂ using N₂ as the carrier gas. The evolved O₂ and H₂ were analyzed on an online GC (GC-2014C, Shimadzu, Kyoto, Japan) equipped with a thermal conductivity detector (TCD) using Ar as the carrier gas.

3.4. Photoelectrochemical Measurement

A photoelectrochemical (PEC) measurement was conducted on an electrochemical workstation (CHI 660D, Chenhua Co., Ltd., Shanghai, China) in a three-electrode quartz glass cell containing 0.5 M K₂SO₄ aqueous solution under a 300 W full-arc Xe lamp irradiation. A piece of Pt wire, an Ag/AgCl electrode, and the photoanode were employed as the counter electrode, reference electrode, and working electrode, respectively.

3.5. COMSOL Multiphysics Simulation

A commercial FEM solver in COMSOL Multiphysics was utilized to simulate the heat distribution in pBT/P25. A two-dimensional (2D) geometry with rotation was built to form a three-dimensional (3D) model, in which the dimensions of the pBT and P25 nanoparticles were the same as the actual sizes obtained from SEM and TEM observations. For simplicity, a single-wavelength infrared light of $\lambda = 800 \text{ nm}$ was selected as the incident light source to solely excite pBT. The simulation was carried out in the atmosphere of CO₂ and H₂O. The heat power volume density (Q_d) is written as [63]:

$$Q_d = 1/2 \epsilon_0 \omega \ln(\epsilon_r) |E|^2 \quad (1)$$

where ϵ_0 is the permittivity of the vacuum, ω is the angular frequency of the light, ϵ_r is the relative permittivity of Bi₂Te₃, and E is the light energy absorbed by Bi₂Te₃, on which the optical properties such as refractive index and absorption coefficient are dependent. All the optical constants of Bi₂Te₃ were obtained from the material library of the software. The results of in situ monitored photothermal temperatures showed that temperatures over P25, pBT, and pBT(x)/P25 could be steady after 40 min. Thus, to provide the numerical value for a temperature gradient, an initial temperature over Bi₂Te₃/TiO₂ composites was set to 100 °C according to the curves of in situ monitored photothermal temperatures at 20 min. Under this condition, the computational complexity of COMSOL software would be reduced, and the results could be similar to the actual temperatures. According to the simulated temperature gradient over Bi₂Te₃/TiO₂ composite, we further calculated the electric potential via COMSOL software. The Seebeck coefficient and electric conductivity were obtained from the manufacturer of pBT (Iuding chemistry Co., Ltd.). During this simulation process, the electric potential at the bottom of the TiO₂ nanoparticle was regarded as zero electric potential.

4. Conclusions

In summary, we used a simple one-step hydrothermal method to successfully fabricate the pBT/P25 nanocomposite exhibiting a remarkably improved activity of CO₂ photoreduction. The highest CO evolution of pBT(2)/P25 ($19.2 \mu\text{mol} \cdot \text{g}_{\text{cat}}^{-1} \cdot \text{h}^{-1}$) was nearly 5.5 times that of P25. The enhancement in the CO₂ photoreduction could be attributed to the following reasons: (i) The Seebeck effect induced a thermoelectric field in pBT for promoting the charge-carrier separation and transfer; (ii) The full-spectrum light absorption capacity

endowed pBT with a photothermal effect to produce a high photothermal temperature for the activation of CO₂ molecules; (iii) The excellent electric conductivity and large work function rendered pBT an efficient cocatalyst to further improve the charge carriers' separation/transfer and reduction ability. Owing to the synergistic enhancement effect in pBT on the activation of CO₂ molecules and the promotion of charge separation/transfer, the CO₂ photoreduction efficiency was significantly enhanced. Our research provides a feasible strategy for the development of an efficient photo-thermo-electro-chemical conversion system for CO₂ reduction based on constructing a full-spectrum responsive thermoelectric material/semiconductor nanocomposite.

Supplementary Materials: The following supporting information can be downloaded at: <https://www.mdpi.com/article/10.3390/catal12111323/s1>, Figure S1: TEM image of pBT(2)/P25; Figure S2: HAADF TEM image and EDS analysis of pBT(2)/P25; Figure S3: SEM images of P25 and pBT(2)/P25; Figure S4: N₂ sorption isotherms of P25 and pBT(2)/P25; Figure S5: XPS spectra of pBT(2)/P25; Figure S6: HR-XPS spectra of Ti 2p, O 1s in pure P25 and pBT(2)/P25, Bi 4f and Te 3d in pure pBT and pBT(2)/P25; Figure S7: GC spectra of CO, CH₄, H₂, and O₂ in CO₂ photoreduction; Figure S8: CO evolution rates over pBT(2)/P25 and pBT(2)/Al₂O₃; Figure S9: In situ monitoring of the photothermal temperatures over pBT(2)/P25 and pBT(2)/Al₂O₃; Figure S10: Light spectra of the Xe lamp with or without a Y44 filter; Figure S11: In situ monitoring of the photothermal temperatures over pBT(2)/P25 under Xe lamp irradiation with and without a Y44 filter; Figure S12: In situ monitoring of the photothermal temperatures over P25 and pBT(2)/P25 under photothermal and cooling conditions; Table S1: Temperatures over P25 and pBT(x)/P25 under photothermal and cooling conditions; Figure S13: CO evolution rates over pBT(x)/P25 under photothermal and cooling conditions; Figure S14: Three cycles of CO₂ photoreduction over pBT(2)/P25; Figure S15: XRD patterns of pBT(2)/P25 before and after reaction; Figure S16: HR-XPS spectra of Ti 2p, O 1s, Bi 4f, and Te 3d in pBT(2)/P25 before and after reaction; Figure S17: In situ monitoring of photoanodes surface temperatures; Table S2: Surface temperatures of P25 and pBT(x)/P25 photoanodes; Figure S18: CO evolution rates over P25 and pBT(x)/P25 under Xe and UV lamps irradiation; Figure S19: In situ monitoring of the photothermal temperatures over pBT(2)/P25 under Xe and UV lamps; Table S3: Comparison of CO₂ photoreduction performance over TiO₂-based photocatalysts. References [64–71] are cited in the supplementary materials.

Author Contributions: Conceptualization, Y.L. and D.W.; methodology and investigation, Y.L., Z.J., and H.H.; writing, Y.L. and D.W.; supervision, D.W.; funding acquisition and resources, D.W., L.L., and J.Y. All authors have read and agreed to the published version of the manuscript.

Funding: This research was funded by the National Natural Science Foundation of China (51572191, 21633004).

Conflicts of Interest: The authors declare no conflict of interest.

References

1. Bibi, M.; Ullah, R.; Sadiq, M.; Sadiq, S.; Khan, I.; Saeed, K.; Zia, M.A.; Iqbal, Z.; Ullah, I.; Iqbal, Z.; et al. Catalytic hydrogenation of carbon dioxide over magnetic nanoparticles: Modification in fixed-bed reactor. *Catalysts* **2021**, *11*, 592. [CrossRef]
2. Zahedi, G.; Elkamel, A.; Lohi, A. Dynamic optimization strategies of a heterogeneous reactor for CO₂ conversion to methanol. *Energy Fuels* **2007**, *21*, 2977–2983. [CrossRef]
3. Shi, L.; Liu, H.; Ning, S.; Ye, J. Localized surface plasmon resonance effect enhanced Cu/TiO₂ core-shell catalyst for boosting CO₂ hydrogenation reaction. *Catal. Sci. Technol.* **2022**, *12*, 6155–6162. [CrossRef]
4. Habisreutinger, S.N.; Schmidt-Mende, L.; Stolarczyk, J.K. Photocatalytic reduction of CO₂ on TiO₂ and other semiconductors. *Angew. Chem. Int. Ed.* **2013**, *52*, 7372–7408. [CrossRef] [PubMed]
5. Zeng, F.; Mebrahtu, C.; Xi, X.; Liao, L.; Ren, J.; Xie, J.; Heeres, H.J.; Palkovits, R. Catalysts design for higher alcohols synthesis by CO₂ hydrogenation: Trends and future perspectives. *Appl. Catal. B Environ.* **2021**, *291*, 120073. [CrossRef]
6. Chang, X.; Wang, T.; Gong, J. CO₂ photo-reduction: Insights into CO₂ activation and reaction on surfaces of photocatalysts. *Energy Environ. Sci.* **2016**, *9*, 2177–2196. [CrossRef]
7. Tan, L.L.; Ong, W.J.; Chai, S.P.; Mohamed, A.R. Photocatalytic reduction of CO₂ with H₂O over graphene oxide-supported oxygen-rich TiO₂ hybrid photocatalyst under visible light irradiation: Process and kinetic studies. *Chem. Eng. J.* **2017**, *308*, 248–255. [CrossRef]

8. Roy, S.C.; Varghese, O.K.; Paulose, M.; Grimes, C.A. Toward solar fuels: Photocatalytic conversion of carbon dioxide to hydrocarbons. *ACS Nano* **2010**, *4*, 1259–1278. [[CrossRef](#)]
9. Zhang, S.; Yin, X.; Zheng, Y. Enhanced photocatalytic reduction of CO₂ to methanol by ZnO nanoparticles deposited on ZnSe nanosheet. *Chem. Phys. Lett.* **2018**, *693*, 170–175. [[CrossRef](#)]
10. Ye, R.P.; Ding, J.; Gong, W.; Argyle, M.D.; Zhong, Q.; Wang, Y.; Russell, C.K.; Xu, Z.; Russell, A.G.; Li, Q.; et al. Double-slit photoelectron interference in strong-field ionization of the neon dimer. *Nat. Commun.* **2019**, *10*, 1.
11. Porosoff, M.D.; Yan, B.; Chen, J.G. Catalytic reduction of CO₂ by H₂ for synthesis of CO, methanol and hydrocarbons: Challenges and opportunities. *Energy Environ. Sci.* **2016**, *9*, 62–73. [[CrossRef](#)]
12. Shanmugaratnam, S.; Selvaratnam, B.; Baride, A.; Koodali, R.; Ravirajan, P.; Velauthapillai, D.; Shivatharsiny, Y. SnS₂/TiO₂ nanocomposites for hydrogen production and photodegradation under extended solar irradiation. *Catalysts* **2021**, *11*, 589. [[CrossRef](#)]
13. Wang, H.; Zhou, D.; Shen, S.; Wan, J.; Zheng, X.; Yu, L.; Phillips, D.L. The photocatalytic activity and degradation mechanism of methylene blue over copper (ii) tetra (4-carboxyphenyl) porphyrin sensitized TiO₂ under visible light irradiation. *RSC Adv.* **2014**, *4*, 28978–28986. [[CrossRef](#)]
14. Dhakshinamoorthy, A.; Navalon, S.; Corma, A.; Garcia, H. Photocatalytic CO₂ reduction by TiO₂ and related titanium containing solids. *Energy Environ. Sci.* **2012**, *5*, 9217. [[CrossRef](#)]
15. Hao, L.; Kang, L.; Huang, H.; Ye, L.; Han, K.; Yang, S.; Yu, H.; Batmunkh, M.; Zhang, Y.; Ma, T. Surface-halogenation-induced atomic-site activation and local charge separation for superb CO₂ photoreduction. *Adv. Mater.* **2019**, *31*, 1900546. [[CrossRef](#)]
16. Chen, F.; Ma, Z.; Ye, L.; Ma, T.; Zhang, T.; Zhang, Y.; Huang, H. Macroscopic spontaneous polarization and surface oxygen vacancies collaboratively boosting CO₂ photoreduction on BiOIO₃ single crystals. *Adv. Mater.* **2020**, *32*, 1908350. [[CrossRef](#)]
17. Wang, Z.; Zhou, W.; Wang, X.; Zhang, X.; Chen, H.; Hu, H.; Liu, L.; Ye, J.; Wang, D. Enhanced photocatalytic CO₂ reduction over TiO₂ using metalloporphyrin as the cocatalyst. *Catalysts* **2020**, *10*, 654. [[CrossRef](#)]
18. Meng, X.; Wang, T.; Liu, L.; Ouyang, S.; Li, P.; Hu, H.; Kako, T.; Iwai, H.; Tanaka, A.; Ye, J. Photothermal conversion of CO₂ into CH₄ with H₂ over group viii nanocatalysts: An alternative approach for solar fuel production. *Angew. Chem. Int. Ed.* **2014**, *53*, 11478–11482. [[CrossRef](#)]
19. Liu, H.; Dao, T.; Liu, L.; Meng, X.; Nagao, T.; Ye, J. Light assisted CO₂ reduction with methane over group VIII metals: Universality of metal localized surface plasmon resonance in reactant activation. *Appl. Catal. B: Environ.* **2017**, *209*, 183–189. [[CrossRef](#)]
20. Meng, X.; Liu, L.; Ouyang, S.; Xu, H.; Wang, D.; Zhao, N.; Ye, J. Nanometals for solar-to-chemical energy conversion: From semiconductor-based photocatalysis to plasmon-mediated photocatalysis and photo-thermocatalysis. *Adv. Mater.* **2016**, *28*, 6781–6803. [[CrossRef](#)]
21. Qi, Y.; Song, L.; Ouyang, S.; Liang, X.; Ning, S.; Zhang, Q.; Ye, J. Photoinduced defect engineering: Enhanced photothermal catalytic performance of 2D black In₂O_{3-x} nanosheets with bifunctional oxygen vacancies. *Adv. Mater.* **2020**, *32*, 1903915. [[CrossRef](#)] [[PubMed](#)]
22. Zhang, J.; Li, Y.; Sun, J.; Chen, H.; Zhu, Y.; Zhao, X.; Zhang, L.; Wang, S.; Zhang, H.; Duan, X.; et al. Regulation of energetic hot carriers on Pt/TiO₂ with thermal energy for photothermal catalysis. *Appl. Catal. B Environ.* **2022**, *133*, 121263. [[CrossRef](#)]
23. Wang, W.; An, W.J.; Ramalingam, B.; Mukherjee, S.; Niedzwiedzki, D.M.; Gangopadhyay, S.; Biswas, P. Size and structure matter: Enhanced CO₂ photoreduction efficiency by size-resolved ultrafine Pt nanoparticles on TiO₂ single crystals. *J. Am. Chem. Soc.* **2012**, *134*, 11276–11281. [[CrossRef](#)]
24. Liu, Z.; Niu, L.; Zong, X.; An, L.; Qu, D.; Wang, X.; Sun, Z. Ambient photothermal catalytic CO oxidation over a carbon-supported palladium catalyst. *Appl. Catal. B Environ.* **2022**, *313*, 121439. [[CrossRef](#)]
25. Soltani, T.; Zhu, X.; Yamamoto, A.; Singh, S.P.; Fudo, E.; Tanaka, A.; Kominami, H.; Yoshida, H. Effect of transition metal oxide cocatalyst on the photocatalytic activity of Ag loaded CaTiO₃ for CO₂ reduction with water and water splitting. *Appl. Catal. B Environ.* **2021**, *52*, 119899. [[CrossRef](#)]
26. Neatu, S.; Macia-Agullo, J.A.; Concepcion, P.; Garcia, H. Gold-copper nanoalloys supported on TiO₂ as photocatalysts for CO₂ reduction by water. *J. Am. Chem. Soc.* **2014**, *136*, 15969–15976. [[CrossRef](#)] [[PubMed](#)]
27. AlOtaibi, B.; Fan, S.; Wang, D.; Ye, J.; Mi, Z. Wafer-level artificial photosynthesis for CO₂ reduction into CH₄ and Co using GaN nanowires. *ACS Catal.* **2015**, *5*, 5342–5348. [[CrossRef](#)]
28. Kang, Q.; Wang, T.; Li, P.; Liu, L.; Chang, K.; Li, M.; Ye, J. Photocatalytic reduction of carbon dioxide by hydrous hydrazine over Au–Cu alloy nanoparticles supported on SrTiO₃/TiO₂ coaxial nanotube arrays. *Angew. Chem. Int. Ed.* **2015**, *54*, 841–845. [[CrossRef](#)]
29. Varghese, O.K.; Paulose, M.; LaTempa, T.J.; Grimes, C.A. High-rate solar photocatalytic conversion of CO₂ and water vapor to hydrocarbon fuels. *Nano Lett.* **2009**, *9*, 731–737. [[CrossRef](#)]
30. Ye, M.; Wang, X.; Liu, E.; Ye, J.; Wang, D. Boosting the photocatalytic activity of P25 for carbon dioxide reduction by using a surface-alkalinized titanium carbide mxene as cocatalyst. *ChemSusChem* **2018**, *11*, 1606–1611. [[CrossRef](#)]
31. Li, J.; Wang, Z.; Chen, H.; Zhang, Q.; Hu, H.; Liu, L.; Ye, J.; Wang, D. A surface-alkalinized Ti₃C₂ MXene as an efficient cocatalyst for enhanced photocatalytic CO₂ reduction over ZnO. *Catal. Sci. Technol.* **2021**, *11*, 4953–4961. [[CrossRef](#)]
32. Li, K.; Chen, T.; Yan, L.; Dai, Y.; Huang, Z.; Guo, H.; Jiang, L.; Gao, X.; Xiong, J.; Song, D. Synthesis of mesoporous graphene and tourmaline co-doped titania composites and their photocatalytic activity towards organic pollutant degradation and eutrophic water treatment. *Catal. Commun.* **2012**, *28*, 196–201. [[CrossRef](#)]

33. Yin, L.; Zhao, M.; Hu, H.; Ye, J.; Wang, D. Synthesis of graphene/tourmaline/TiO₂ composites with enhanced activity for photocatalytic degradation of 2-propanol. *Chin. J. Catal.* **2017**, *38*, 1307–1314. [[CrossRef](#)]
34. Pang, F.; Zhang, R.; Lan, D.; Ge, J. Synthesis of magnetite-semiconductor-metal trimer nanoparticles through functional modular assembly: A magnetically separable photocatalyst with photothermic enhancement for water reduction. *ACS Appl. Mater. Interfaces* **2018**, *10*, 4929–4936. [[CrossRef](#)]
35. Tan, J.; Wang, X.; Hou, W.; Zhang, X.; Liu, L.; Ye, J.; Wang, D. Fabrication of Fe₃O₄@graphene/TiO₂ nanohybrid with enhanced photocatalytic activity for isopropanol degradation. *J. Alloy Compd.* **2019**, *792*, 918–927. [[CrossRef](#)]
36. Li, F.; Wang, H.; Huang, R.; Chen, W.; Zhang, H. Recent advances in SnSe nanostructures beyond thermoelectricity. *Adv. Funct. Mater.* **2022**, *32*, 2200516. [[CrossRef](#)]
37. Ji, Y.; Yang, M.; Dong, H.; Wang, L.; Hou, T.; Li, Y. Monolayer group IVA monochalcogenides as potential and efficient catalysts for the oxygen reduction reaction from first-principles calculations. *J. Mater. Chem. A* **2017**, *5*, 1734. [[CrossRef](#)]
38. Rajamathi, C.R.; Gupta, U.; Pal, K.; Kumar, N.; Yang, H.; Sun, Y.; Shekhar, C.; Yan, B.; Parkin, S.; Waghmare, U.V.; et al. Photochemical water splitting by bismuth chalcogenide topological insulators. *ChemPhysChem* **2017**, *18*, 2322–2327. [[CrossRef](#)]
39. Li, X.; Zuo, X.; Jiang, X.; Li, D.; Cui, B.; Liu, D. Enhanced photocatalysis for water splitting in layered tin chalcogenides with high carrier mobility. *Phys. Chem. Chem. Phys.* **2019**, *21*, 7559. [[CrossRef](#)]
40. Wu, Q.; Wei, W.; Lv, X.; Huang, B.; Dai, Y. Computational screening of defective group IVA monochalcogenides as efficient catalysts for hydrogen evolution reaction. *J. Phys. Chem. C* **2019**, *123*, 11791–11797. [[CrossRef](#)]
41. Chen, P.; Dai, X.; Xing, P.; Zhao, X.; Zhang, Q.; Ge, S.; Si, J.; Zhao, L.; He, Y. Microwave heating assisted synthesis of novel SnSe/g-C₃N₄ composites for effective photocatalytic H₂ production. *J. Ind. Eng. Chem.* **2019**, *80*, 74. [[CrossRef](#)]
42. Wu, D.; Guo, J.; Ge, Z.; Feng, J. Facile Synthesis Bi₂Te₃ based nanocomposites: Strategies for enhancing charge carrier separation to improve photocatalytic activity. *Nanomaterials* **2021**, *11*, 3390. [[CrossRef](#)] [[PubMed](#)]
43. Zhang, N.; Zheng, F.; Huang, B.; Ji, Y.; Shao, Q.; Li, Y.; Xiao, X.; Huang, X. Exploring Bi₂Te₃ nanoplates as versatile catalysts for electrochemical reduction of small molecules. *Adv. Mater.* **2020**, *32*, 1906477. [[CrossRef](#)]
44. Shim, X.; Zou, J.; Chen, Z. Advanced thermoelectric design: From materials and structures to devices. *Chem. Rev.* **2020**, *120*, 7399–7515.
45. Ryu, B. Work function of bismuth telluride: First-principles approach. *J. Korean Phys. Soc.* **2018**, *72*, 122–128. [[CrossRef](#)]
46. Chen, X.; Liu, L.; Huang, F. Black titanium dioxide (TiO₂) nanomaterials. *Chem. Soc. Rev.* **2015**, *44*, 1861–1885. [[CrossRef](#)]
47. Wu, Y.; Lu, G.; Li, S.J. The doping effect of Bi on TiO₂ for photocatalytic hydrogen generation and photodecolorization of rhodamine B. *J. Phys. Chem. C* **2009**, *113*, 9950–9955. [[CrossRef](#)]
48. Patil, P.; Mali, S.; Kondalkar, V.; Mane, R.; Patil, P.S.; Hong, C.; Bhosale, P. Bismuth telluride quantum dot assisted titanium oxide microflowers for efficient photoelectrochemical performance. *Mater. Lett.* **2015**, *159*, 177–181. [[CrossRef](#)]
49. Kim, S.; We, J.; Cho, B. A wearable thermoelectric generator fabricated on a glass fabric. *Energy Environ. Sci.* **2014**, *7*, 1959–1965. [[CrossRef](#)]
50. Yang, L.; Wang, C.; Lin, S.; Chen, T.; Cao, Y.; Zhang, P.; Liu, X. Thermal conductivity of TiO₂ nanotube: A molecular dynamics study. *J. Phys.: Condens. Matter* **2019**, *31*, 055302. [[CrossRef](#)]
51. Muñoz Rojo, M.; Abad, B.; Manzano, C.; Torres, P.; Cartoixa, X.; Alvarezb, F.; Martín Gonzalez, M. Thermal conductivity of Bi₂Te₃ nanowires: How size affects phonon scattering. *Nanoscale* **2017**, *9*, 6741–6747. [[CrossRef](#)] [[PubMed](#)]
52. Lu, X.; Jiang, P.; Bao, X. Phonon-enhanced photothermoelectric effect in SrTiO₃ ultra-broadband photodetector. *Nat. Commun.* **2019**, *10*, 138. [[CrossRef](#)] [[PubMed](#)]
53. Bell, L. Cooling, heating, generating power, and recovering waste heat with thermoelectric systems. *Science* **2008**, *321*, 1457–1461. [[CrossRef](#)] [[PubMed](#)]
54. Chen, T.; Guai, G.H.; Gong, C.; Hu, W.; Zhu, J.; Yang, H.; Yan, Q.; Li, C. Thermoelectric Bi₂Te₃-improved charge collection for high-performance dye-sensitized solar cells. *Energy Environ. Sci.* **2012**, *5*, 6294–6298. [[CrossRef](#)]
55. He, H.; Zhang, C.; Liu, T.; Cao, Y.; Wang, N.; Guo, Z. Thermoelectric–photoelectric composite nanocables induced a larger efficiency in dye-sensitized solar cells. *J. Mater. Chem. A* **2016**, *4*, 9362–9369. [[CrossRef](#)]
56. Jia, Z.; Ning, S.; Tong, Y.; Chen, X.; Hu, H.; Liu, L.; Ye, J.; Wang, D. Selective photothermal reduction of CO₂ to CO over Ni-nanoparticle/N-doped CeO₂ nanocomposite catalysts. *ACS Appl. Nano Mater.* **2021**, *4*, 10485–10494. [[CrossRef](#)]
57. Li, Z.; Liu, J.; Shi, R.; Waterhouse, G.I.N.; Wen, X.; Zhang, T. Fe-based catalysts for the direct photohydrogenation of CO₂ to value-added hydrocarbons. *Adv. Energy Mater.* **2021**, *11*, 2002783. [[CrossRef](#)]
58. Han, B.; Wei, W.; Chang, L.; Cheng, P.; Hu, Y. Efficient visible light photocatalytic CO₂ reforming of CH₄. *ACS Catal.* **2016**, *6*, 494–497. [[CrossRef](#)]
59. Zhang, X.; Wang, X.; Wang, D.; Ye, J. Conformal BiVO₄-layer/WO₃-nanoplate-array heterojunction photoanode modified with cobalt phosphate cocatalyst for significantly enhanced photoelectrochemical performances. *ACS Appl. Mater. Interfaces* **2019**, *11*, 5623–5631. [[CrossRef](#)]
60. Chen, Y.; Chen, H.; Ku, S.; Luo, C.; Lin, J.; Wu, K.; Juang, J.; Kobayashi, T.; Cheng, C.; Tsuei, K.; et al. Manifestation of a second dirac surface state and bulk bands in THz radiation from topological insulators. *Sci. Rep.* **2015**, *5*, 14128.
61. Subramanian, V.; Wolf, E.E.; Kamat, P.V. Catalysis with TiO₂/Gold nanocomposites. Effect of metal particle size on the fermi level equilibration. *J. Am. Chem. Soc.* **2004**, *126*, 4943–4950. [[CrossRef](#)] [[PubMed](#)]

62. Jakob, M.; Levanon, H.; Kamat, P.V. Charge distribution between UV-Irradiated TiO₂ and gold nanoparticles: Determination of shift in the fermi level. *Nano Lett.* **2003**, *3*, 353–358. [[CrossRef](#)]
63. Liu, J.; Zhang, Y.; Wang, Z.; Li, M.; Su, W.; Zhao, M.; Huang, S.; Xia, S.; Wang, C. Accurate measurement of Seebeck coefficient. *Rev. Sci. Instrum.* **2016**, *87*, 064701. [[CrossRef](#)] [[PubMed](#)]
64. Li, Y.; Walsh, A.G.; Li, D.; Do, D.; Ma, H.; Wang, C.; Zhang, P.; Zhang, X. W-Doped TiO₂ for photothermocatalytic CO₂ reduction. *Nanoscale* **2020**, *12*, 17245–17252. [[CrossRef](#)]
65. Li, G.; Sun, Y.; Zhang, Q.; Gao, Z.; Sun, W.; Zhou, X. Ag quantum dots modified hierarchically porous and defective TiO₂ nanoparticles for improved photocatalytic CO₂ reduction. *Chem. Eng. J.* **2021**, *410*, 128397. [[CrossRef](#)]
66. Sun, Y.; Li, G.; Gong, Y.; Sun, Z.; Yao, H.; Zhou, X. Ag and TiO₂ nanoparticles co-modified defective zeolite TS-1 for improved photocatalytic CO₂ reduction. *J. Hazard. Mater.* **2021**, *403*, 124019. [[CrossRef](#)]
67. Xing, M.; Zhou, Y.; Dong, C.; Cai, L.; Zeng, L.; Shen, B.; Pan, L.; Dong, C.; Chai, Y.; Zhang, J.; et al. Modulation of the reduction potential of TiO_{2-x} by fluorination for efficient and selective CH₄ generation from CO₂ photoreduction. *Nano Lett.* **2018**, *18*, 3384–3390. [[CrossRef](#)]
68. Feng, S.; Zhao, J.; Bai, Y.; Liang, X.; Wang, T.; Wang, C. Facile synthesis of Mo-doped TiO₂ for selective photocatalytic CO₂ reduction to methane: Promoted H₂O dissociation by Mo doping. *J. CO₂ Util.* **2020**, *38*, 1–9. [[CrossRef](#)]
69. Bian, J.; Qu, Y.; Zhang, X.; Sun, N.; Tang, D.; Jing, L. Dimension-matched plasmonic Au/TiO₂/BiVO₄ nanocomposites as efficient wide-visible-light photocatalysts to convert CO₂ and mechanistic insights. *J. Mater. Chem. A* **2018**, *6*, 11838–11845. [[CrossRef](#)]
70. Xu, F.; Meng, K.; Cheng, B.; Wang, S.; Xu, J.; Yu, J. Unique S-scheme heterojunctions in self-assembled TiO₂/CsPbBr₃ hybrids for CO₂ photoreduction. *Nat. Commun.* **2020**, *11*, 4613. [[CrossRef](#)]
71. He, F.; Zhu, B.; Cheng, B.; Yu, J.; Ho, W.; Macyk, W. 2D/2D/0D TiO₂/C₃N₄/Ti₃C₂ MXene composite S-scheme photocatalyst with enhanced CO₂ reduction activity. *Appl. Catal. B* **2020**, *272*, 119006. [[CrossRef](#)]